Low-Current Hollow Cathode Evaluation

Matthew T. Domonkos*, Alec D. Gallimore†, and George J. Williams, Jr.‡
Plasmadynamics and Electric Propulsion Laboratory (PEPL)
The University of Michigan
Ann Arbor, MI 48109

Michael J. Patterson§
NASA Glenn Research Center
Cleveland, OH 44135

Abstract

An experimental investigation of the operating characteristics of 3.2 mm diameter orificed hollow cathodes was conducted to examine low-current and low flow rate operation. Cathode power was minimized with low orifice aspect ratio and the use of an enclosed keeper. Cathode flow rate requirements were proportional to orifice diameter and the inverse of the orifice length. Cathode temperature profiles were obtained using an imaging radiometer, and conduction was found to be the dominant heat transfer mechanism from the cathode tube. Orifice plate temperatures were found to be weakly dependent upon the flow rate and strongly dependent upon the current. Internal cathode pressures were measured to range from 39.2 to more than 66.5 kPa for spot mode emission. A model developed to describe the mass flow achieved good agreement with the experimental cathode pressures for heavy particle temperatures between 2900 and 6100 ºC. Plasma properties measured within the insert region exclude the electron partial pressure from being responsible for the elevated cathode pressures. As such, it was concluded that the average heavy particle temperature in the orifice would have to be on the order of several thousand degrees C to account for the high internal pressure. Plasma parameters were also measured in the cathode-to-keeper gap and downstream of the keeper. The structure of the data enabled analysis of the current conduction processes in spot and plume modes.

Nomenclature

A	= normalization coefficient	p	= pressure, Pa
AR*x*	= cathode with an orifice aspect ratio of *x*	p_c	= critical sonic pressure, Pa
$\vec{B}$	= magnetic field vector, G	p_{in}	= insert region pressure, Pa
b	= coefficient in EEDF exponent	p_o	= orifice region pressure, Pa
D_o	= orifice diameter, m	R	= orifice radius, m
E	= electron energy, eV	$\tilde{R}$	= Ideal gas constant, 8.3145 J/mol-K
EEDF	= electron energy distribution function	$\bar{u}$	= mean flow velocity, m/s
f(E)	= normalized EEDF	V_o	= velocity at the orifice exit, m/s
I_{pr}	= probe current, A	V_p	= plasma potential, V
$\vec{J}$	= current density vector, A/m^2	V_{pr}	= probe voltage, V
K_L	= coefficient of loss	x	= axial distance, m, or exponent on electron energy in EEDF
L_o	= orifice length, m	γ	= ratio of specific heats, 5/3
M	= molar mass of Xe, 131 g/mol	μ	= dynamic viscosity, N-s/m^2
$\dot{m}$	= mass flow rate, kg/s		

* Graduate Student Research Assistant, Student Member AIAA
† Associate Professor, Associate Fellow AIAA
‡ Graduate Student Research Assistant, Student Member AIAA
§ Research Scientist, Member AIAA

Copyright © 1999 by Matthew T. Domonkos. Published by the American Institute of Aeronautics and Astronautics with permission.

Introduction

While state-of-the-art electric propulsion systems provide a clear advantage compared with chemical thrusters for stationkeeping and some primary propulsion applications on satellites with several kilowatts of power generation, electric thrusters currently require performance improvements before they become a viable option for small satellite propulsion.[1] The performance of low-power, sub-300 W, ion and Hall thrusters depends heavily upon the power and propellant consumed by the hollow cathode neutralizer;[1] the cathode in the Hall thruster performs the functions of both main discharge cathode and beam neutralizer. Patterson and Oleson[1] reported that the neutralizer for a 100-W ion thruster could degrade the efficiency by up to 20 percent and reduce the specific impulse by as much as 2000 seconds. Optimization of hollow cathodes is also sought for plasma contactor applications. The design of hollow cathodes for low-power thrusters requires optimization of the propellant flow and power required for steady, spot-mode emission. While neutralizers for ion and Hall thrusters can be operated in plume mode, the coupling voltage is greatly increased, and the discharge oscillations inherent in plume mode have been linked to cathode erosion and thruster instabilites.[2] In order to develop design tools, an initial experimental investigation was conducted using laboratory model cathodes to determine the similarities and differences of low-power hollow cathode operation with previous studies.[3,4,5] This paper reports the results of the experimental investigation of laboratory model 3.2-mm diameter orificed hollow cathodes for low-current applications.

Some of the earliest work with orificed-hollow cathodes for electric propulsion devices was conducted by researchers at the NASA Glenn Research Center (GRC), formerly Lewis Research Center, and Hughes Research Laboratories (HRL) beginning in the 1960's.[2,5,6,7,8] The initial development work focused on the neutralizer hollow cathode for the Space Electric Rocket Test II (SERT II) mercury ion thruster. Rawlin and Pawlik characterized the operation in spot and plume modes and established that the cathode performance was insensitive to orifice aspect ratio, defined as the length divided by the diameter, for values up to four.[5] Byers and Snyder determined that cathode power scaled inversely with keeper and collector surface area visible from the orifice exit.[6] An investigation performed at the Jet Propulsion Laboratory (JPL) in 1971 determined the cathode tube temperature distribution experimentally and analytically.[9] Mirtich reported the findings of an investigation into orifice plate erosion and temperature distributions in hollow cathodes for 30-cm ion thrusters in 1973.[8] Rawlin also reported on the results of a 13,000 hour life test of a mercury hollow cathode in 1973.[2] The orifice plate had eroded from the downstream end, and Rawlin hypothesized that the erosion was caused by high-energy ions created during the large voltage oscillations in plume mode.[2] Experimental investigations of hollow cathodes at NASA GRC, HRL, and JPL have continued to the present, and several efforts to model hollow cathode processes were reported or started in the 1970's.[3,10,11,12,13,14,15]

Much of the cathode development work with inert gases has focused on operation at several Amperes and higher with flows of at least 2 sccm (~0.2 mg/s for xenon).[4,11,12,14,15] Historically these operating regimes have been driven by the emission requirements of ion thrusters, and later plasma contactors. The NASA Solar Electric Propulsion Test And Readiness (NSTAR) program brought the NASA ion engine to a state of flight qualification, and the discharge and neutralizer hollow cathodes were qualified as a result. Similarly, the requirements for the plasma contactor on the International Space Station (ISS) led to various life tests of 6.4-mm diameter hollow cathodes for use at up to 10 A continuously. These developments have benefited interplanetary spacecraft by enabling sample return missions with ion thrusters and extended the payload capacity for communications satellites using Hall or ion thrusters. For small satellites to employ electric propulsion effectively, similar performance and lifetimes must be demonstrated at low-current and low-flow rates. Since 1995 3.2-mm diameter, low-flow rate hollow cathodes have been under development at the GRC for use with low-power ion and Hall thrusters, as well as plasma contactors.

This paper reports the findings of an experimental investigation of laboratory model 3.2-mm diameter hollow cathodes which were designed based largely on previously developed scaling relations. Cathode performance was characterized on several cathodes with varying orifice geometry to evaluate the current state-of-the-art. A detailed thermal analysis of the cathode was performed, and the plasma properties were mapped to evaluate the current conduction mechanisms. The major conclusions of this investigation are summarized, and the optimization of cathode design for low-current is discussed.

Experimental Apparatus

The hollow cathodes used in this investigation were designed and fabricated based loosely on existing hollow cathode and plasma contactor procedures.[16,17] Since the cathodes were laboratory models, a number of the specifications and inspection procedures required for flight hardware were either relaxed or omitted. The authors attempted to follow the flight hardware procedures when it was reasonable to do so, in order to facilitate the transition from laboratory models to flight units.

Hollow Cathode Design

An engineering schematic of the 3.2-mm diameter hollow cathodes is presented in Figure 1, and the identifying characteristics of the various cathodes tested are listed in Table 1. The materials used for the cathode were consistent with plasma contactor and ion thruster cathodes.[16] Citing export regulations, the GRC has requested that the exact dimensions and materials of the cathode assemblies be omitted here; United States' companies, universities, and government agencies may request this information from the authors. The orifice diameter for the first cathodes was chosen based on the Kaufman criterion of 12 A/mm of orifice diameter.[18] The orifice length was chosen by combining machining considerations with numerical results obtained from the model by Mandell and Katz.[19] The resulting orifice had a length-to-diameter aspect ratio of approximately six, and the two cathodes made with this type of orifice are referred to as AR6 and AR6´. Cathodes with orifice aspect ratios of approximately three (AR3) and one (AR1) were also constructed, and the three geometries are depicted to scale in Figure 2. A cathode with an aspect ratio of three (AR3´) was constructed with an orifice diameter sixty percent that of AR6, and hence lower current carrying capability. Finally, a third cathode with orifice plate dimensions identical to AR6 and AR6´ was constructed for tests in both enclosed (EK6) and open keeper (OK6) configurations as shown in Figure 3. Excluding the use of either an enclosed keeper or a mesh keeper for some tests, the keeper geometry and gap were held constant in this investigation. The insert dimensions were set by the availability of Ion Auxiliary Propulsion System (IAPS) program hardware.

Facilities

Three vacuum facilities were used in this investigation: 1) Port 2 of Tank 11 at GRC, 2) Vacuum Facility 52 at GRC, and the Cathode Test Facility (CTF) at the Plasmadynamics and Electric Propulsion Laboratory (PEPL). The CTF is depicted schematically in Figure 4. All of these facilities were cryopumped, and Port 2 and CTF have base pressures in the high-10^{-6} Pa range. During cathode operation, the tank pressure in all three facilities varied from 3 to 11 x 10^{-3} Pa. In each case, 99.999 percent pure xenon was supplied to the cathode through a flow system accurate to within ±0.07 sccm based upon bubble flow-meter calibrations and with a leak rate calibrated to be less than 1.5 x 10^{-5} sccm.

Cathode Performance

When attempting to assess experimentally the effects of varying the orifice geometry on the performance of hollow cathodes, the ideal technique is to change only the orifice plate. This was done by Siegfried,[3] using a slide valve with three orifice geometries. The experiment was conducted on a mercury hollow cathode, and the aspect-ratios (L_o/D_o) of the orifices were negligibly small in comparison with those considered in the current investigation. A similar experiment performed with the aspect-ratios of interest would have been feasible. However, throughout the current investigation, the experiments were designed for hollow cathode assemblies which could easily be integrated with a thruster. Consequently, to test the effects of varying the orifice aspect-ratio on the performance of the cathode, separate assemblies were fabricated and tested. In order to validate that the observed changes in performance were due to orifice geometry changes, it was necessary examine the operating variance between cathodes fabricated to identical specifications.

For reference, the work on the ISS plasma contactor has demonstrated variances of ±0.5-V above 7-sccm of Xe, increasing to approximately ±1.0-V around 5-sccm.[16] The flow rate where the spot-to-plume mode transition occurred appeared to be invariant.[16] Sarver-Verhey[20] demonstrated that over the life of a 6.4-mm diameter cathode, the operating voltage for a given flow rate and current can vary by at least ±1.0-V. It should be noted that the fluctuations referred to here occur over many tens to thousands of hours.

The voltage-flow rate characteristics of two mechanically identical cathodes, AR6 and AR6´, at 1.25-A are presented in Figure 5. The characteristics show a variance of approximately ±1.0-V in the spot-mode regime, and the transition flow rate varied by as much as 0.4-sccm. These variances were typical of those observed throughout the range of operating conditions evaluated. The keeper voltage fluctuations for individual cathodes were examined over the course of tens of hours and were found to be on the order of 0.2-V when operated at constant current and flow rate. Inspection of Figure 5 shows that the variance between subsequent characterizations was on the order of 0.2-V. This effect was attributed to changes in the insert chemistry which occurred at differing rates depending upon cathode operating conditions between the performance characterizations. The transition flow rate generally increased with time. This effect was attributed to an increase in the orifice diameter, and comparison of microscopic images of the orifice supported this conclusion. Given that similar fabrication and operating procedures were employed with both the 3.2-mm diameter hollow cathodes and the ISS plasma contactors, the variance exhibited in Figure 5 was taken to be a reasonable representation of the performance variance expected with these cathodes. Consequently, the overall voltage and transition flow rate variances were taken to be ±1.4-V and ±0.25 sccm.

The variation noise, differences between cathodes manufactured from the same specifications, could be minimized by rigidly attaching the insert to the cathode tube. As a consequence of the fabrication technique followed for the cathodes tested in this investigation, the axis of the insert may be misaligned with the orifice axis. Figure 6 illustrates that the worst case results in a misalignment of the axes by 16 percent of the insert diameter. The relaxed specification on the insert outer diameter introduced an indeterminant mechanical alteration between cathodes and contributed to the variation noise shown in Figure 5.

Minimizing Power In a Diode Discharge

Most of the experiments reported in this paper involved diode discharges between a hollow cathode and a keeper, and cathode power was defined as the product of the cathode-to-keeper voltage and current. By focusing on a diode discharge, comparison between the performance of the hollow cathodes was straightforward. This approach assumes that the total emission current, the sum of the keeper and secondary anode emission currents, dominates the conditions at the cathode, regardless of the distribution of the current to the anodes. The tests were conducted by varying the flow rate at constant current.

Figure 7 illustrates a typical performance characterization. The portion of the curves where the voltage is only weakly dependent upon the flow rate is known as spot mode. Spot mode is also characterized by having a small AC component in the current and voltage, and a small luminous "spot" at the orifice of the cathode.[5] Plume mode by contrast has a luminous "plume" that extends downstream to the keeper and beyond, and the AC component of the current and voltage becomes a large fraction of the DC values. The spot and plume mode current and voltage oscillations for AR3 appear in Figure 8. The period of the oscillations in plume-mode was far shorter, 200 ns, than the transient response time of the regulated DC power supply, 50 μs, used to drive the discharge. The magnitude of the voltage oscillations appeared to be limited only by the output capability of the power supply. With the voltage fluctuating between zero and 60-V, ions created in the cathode-keeper gap will be accelerated toward the cathode at up to 60-V, as postulated by Rawlin.[2]

Spot-mode emission at orifice plate temperatures below 1300 ºC was chosen as an operational limit for these experiments to be consistent with practices proven to enable lifetimes greater than 10,000 hours.[20] The cathode tip temperature has been considered that which is the most closely related to the insert temperature.[4,20] If the temperature is too high, the barium in the insert evaporates more quickly than it can be replenished through diffusion, and the discharge becomes unstable; low temperatures are insufficient to drive the chemical reactions at a rate that sustains the low work function surface of the emitter.[21] Since the lower limit represents a non-destructive condition, the cathodes were operated at as low of an orifice plate temperature as stable operation permitted. The upper limit of 1300 ºC corresponded well with the Kaufman limit of 12 A/mm of orifice diameter for AR6 and AR6´.[18] AR1 operated significantly beyond the Kaufman limit while the orifice plate temperature remained below 1300 ºC.

The performance characterizations were conducted at intervals of several tens of hours of operation to obtain a more representative assessment of the cathode operating regimes than from a single characterization. Detailed information on the cathode performance appears in Domonkos, Gallimore, and Patterson.[22,23] It should be noted that the flow rates as reported in Reference [22] were approximately 50 percent low (i.e., 0.5 sccm reported was actually

1.0 sccm) due to an inaccurate calibration by other researchers. This report only presents results for which the flow rate calibration was performed by the authors.

As Figure 7 shows, for a given current, a certain minimum flow rate is required to maintain spot mode emission. Cathode power consumption at the minimum flow rate condition for spot-mode emission is plotted as a function of the discharge current in Figure 9. When comparing AR1, AR3, and AR6´, the smallest aspect-ratio cathode consumed the least amount of power at a given current. While this result was expected since power scales with orifice length according to Ohms law, AR3 and AR6´ operated at roughly equal power levels throughout the range of currents. This result suggests that the change in power consumption with orifice length occurs more rapidly at low aspect-ratios. The power consumption for AR1 was the lowest of all the cathodes tested. Changing the orifice diameter resulted in a negligible change in the power consumption as evidenced by Figure 9b. The use of an enclosed keeper reduced the power requirement on the order of five to ten percent over the open keeper configuration. Since the enclosed keeper provides a superior radiation environment, the small improvement in power consumption by using the enclosed keeper suggests that conduction was the dominant heat transfer mechanism for the cathode tube; if the open keeper were radiating strongly, the enclosed keeper would improve the performance more significantly than observed. The operating temperature must also be taken into account in making this statement, and the results of a thermographic analysis are presented later.

The flow rate required for spot mode emission, plotted in Figure 10, also strongly influences efficiency in low-power thrusters. The model by Mandell and Katz[19] predicts that ion production within the orifice, and consequently ion flux out of the orifice, increase with orifice length for a given diameter and flow rate. As the orifice length is increased, the electron temperature in the orifice also increases due to Ohmic heating. The elevated electron temperature and increased channel length facilitate ionization. The transition to plume mode operation occurs when the ion flux from the orifice is insufficient to maintain charge neutrality in the cathode-keeper gap. Figure 10a shows that the model predictions were consistent with the trends observed for aspect-ratios between 1 and 6. The AR6´ and AR3 cathodes appeared to transition at approximately the same flow rates, suggesting diminishing returns in optimizing the transition flow rate by increasing the orifice length. Indeed, one must also consider the ion losses as the orifice aspect-ratio is increased. The results in Figure 10b demonstrated the expected trend that as orifice diameter decreases, the flow rate required for spot-mode operation also decreases. The increased current density within the orifice facilitates ion production and emission; ion emission occurs by ambipolar diffusion outside of the cathode sheath and may constitute several mA of current. The transition flow rate was less for the open keeper configuration than for the enclosed keeper. This result was unexpected because the pressure in the cathode-keeper gap is expected to be greater with the enclosed keeper, thereby facilitating ion transport by reducing the cathode sheath size. An increase in the neutral density in the cathode-to-keeper gap also impedes the flow of ions through collisions with neutrals, an adverse condition for the enclosed keeper.

Electron Emission Characteristics

A secondary, planar anode 48 mm in diameter was placed 60-mm downstream to assess the electron emission capability of the 3.2-mm diameter hollow cathodes. The flow was set to the minimum for spot-mode operation in a diode discharge, and the secondary anode was biased with respect to the cathode. The resulting characteristics are shown in Figure 11. Despite decreasing flow rates, the emission current scaled with the keeper current. Additionally, current saturation appeared to set in at a bias of approximately 20-V. The AR3 cathode with a mesh keeper yielded emission currents of 0.17-A at 20-V and 0.30-A at 24-V with a 0.75-A keeper current at 2.4 sccm. Since the mesh keeper and orifice geometry were expected to contribute weakly to the change in emission current, the effect of increasing the flow at 0.75-A to the keeper was established; an increase of 0.6 sccm led to a 100 percent increase in the emission current.

Cathode Operating Pressure

While cathode performance and emission capabilities are the primary concerns for the overall thruster design, the cathode pressure when combined with plasma diagnostics enables a detailed physical picture of the cathode processes to be developed. Salhi[4] found that the pressure in a 6.4-mm diameter cathode with a 1.21-mm diameter orifice was approximately 665 Pa on xenon at operating conditions similar to those reported here. As an approximation, the cathode pressure scales as the ratio of the orifice areas. Given the data from Salhi,[4] the

enclosed/open keeper cathode, AR1, AR3, AR6, and AR6´ were expected to operate in the range of 40 kPa. The cathode operating pressures for EK6 and AR3 are plotted in Figure 12. Both cathodes were operated in diode mode for these data, and the pressure scaled strongly with the flow rate at all of the discharge currents. Between 1.00-A and 1.50-A, the pressure appeared to be more weakly dependent upon current than below 1.00-A. For the enclosed keeper cathode, the transition to plume mode occurred at approximately 39.2 kPa regardless of the current and flow rate. The argument that the pressure scales principally with orifice area fails to account for the reduced pressure operation of AR3 compared with EK6, which has an identical orifice diameter; cathode pressure is also proportional to orifice length. Conceptually this is reasonable when one considers the pressure required to flow gas through two of the orifice geometries depicted in Figure 2.

To assess the cathode pressure as a function of neutral flow, the cathode pressure was monitored while flowing xenon in the absence of a discharge at room temperature and with an orifice plate temperature of 955 ºC, maintained by the cathode heater. Figure 12 also shows the pressure variation with neutral flows for EK6 at room temperature (25 ºC) and at 955 ºC. The xenon was assumed to be in equilibrium with the cathode orifice temperature. The discharge processes account for the increase in pressure of approximately 200 percent over a neutral flow at 955 ºC. The start-up transients are depicted in Figure 13 to illustrate the effect of the discharge on cathode pressure. Initially, the cathode was starved for propellant and operated in plume mode, while the propellant feed line between the metering valve and the cathode pressurized. The facility pressure was also observed to decrease upon ignition, indicating that a significant fraction of the flow was involved in raising the cathode internal pressure. Approximately three minutes after ignition, the cathode pressure was sufficient (~39.2 kPa) to transition to spot mode. The cathode took more than 7 minutes to reach a steady state pressure. In this particular case, the cathode tip temperature dropped 170 ºC transitioning from the preheat condition to a steady discharge. Despite an orifice plate temperature of 760 ºC, the presence of the discharge drove the cathode pressure to more than twice that observed with a purely neutral flow at 955 ºC.

Several plasma related phenomena have the potential for increasing the internal pressure. If the electron number density were high enough, then the electron partial pressure may be responsible. However, based on the Langmuir probe analysis of the insert plasma presented later, the electron partial pressure was at most 22.4 Pa in the insert region, and an electron partial pressure of 4.89 kPa in the orifice was calculated using the code by Mandell and Katz.[19] A calculation of the pinch effect, $\vec{J}\times\vec{B}$, in the orifice region led to a pressure on the order of 8 Pa. Having eliminated the electron partial pressure as responsible for the total pressures presented in Figure 12, the heavy particle temperature was determined to be the driver.

Several authors have argued for using the cathode wall temperature as an approximation of the neutral and ion temperatures in hollow cathodes.[3,10] On the other hand, Salhi[4] developed a model to predict the radial variation in heavy particle temperatures within the hollow cathode. The model showed that at high current, or more generally high current density, the heavy particle temperature on axis varied greatly from the wall temperature and could be a fraction of an electron Volt. Salhi's[4] calculations focused on the insert region, however, the current density is greatest in the orifice of the hollow cathode. Since the cathode pressure increases as the tip temperature decreases in Figure 13, the heavy particle temperature in the cathode was expected to differ from the cathode tip temperature by several hundred to several thousand degrees C.

An empirical means to estimate the mean particle temperature is to model the flow through the orifice. In order to create a predictive model, an expression for the pressure must be derived which limits the use of empirical relations. Salhi[4] introduced an expression based on isothermal flow in the cathode with a sonic condition at the exit of the orifice. Here, an expression is derived which includes elements from Salhi[4] with consideration of the effects of a finite length orifice. It should be noted that the mass flow equations reported by Salhi[4] contain errors which have been corrected in the present derivation.

The Reynolds numbers were below five for the cases expected in the 3.2-mm diameter cathodes. The Knudsen numbers were calculated to be less than 0.13 and 0.02 in the orifice and insert regions, respectively. Consequently, this region was modeled using continuum Poiseuille flow. The average velocity expression for Poiseuille flow is,

$$\bar{u} = \frac{R^2}{8\mu}\left(-\frac{dp}{dx}\right) \quad (1)$$

The pressure gradient in Eqn. 1 was linearized. At the low flow velocity in the cathode, the pressure drop along the cathode tube is negligible compared with the drop across the orifice. Consequently, the reference pressure must be in the orifice. The result when put into the continuity equation is an expression for the mass flow rate as a function of the pressure p(x):

$$\dot{m} = \frac{\pi R^4}{8\mu}\frac{M}{\tilde{R}T}\frac{p_o + p(x)}{2}\frac{p(x) - p_o}{x} \quad (2)$$

from which we can solve for p(x):

$$p(x) = \left[\dot{m}\frac{8\mu}{\pi R^4}\frac{\tilde{R}T}{M}(2x) + p_o^2\right]^{0.5} \quad (3)$$

This leaves p_o and the temperature unknown. The continuity equation and a choked flow condition at the exit of the orifice lead to the following relation:

$$p_c = \dot{m}\frac{\tilde{R}T}{M}\frac{1}{\pi R^2}\sqrt{\frac{M}{\gamma\tilde{R}T}} \quad (4)$$

By equating p_c with p_o, the pressure at the exit of the orifice is determined for a given gas temperature. To account for the pressure drop across the orifice entrance, an isothermal energy equation is used

$$p_{in} = p_x + \tfrac{1}{2}\rho_o V_o^2(1 + K_L) \quad (5)$$

where p_{in} is the pressure in the insert region, and K_L=0.5 is the coefficient of loss at the orifice entrance.[24]

This expression was used to model the pressure measured in the hollow cathode with a neutral flow, and the comparison is depicted in Figure 14. In this case, using the cathode tube temperature as the gas temperature under predicted the cathode pressure. Agreement between the model and the data was obtained by using a slightly higher temperature than was observed. At elevated temperatures, it is reasonable to expect a significant temperature gradient across the orifice plate which could be responsible for the deviation between experiment and prediction. The model predicted the flow at room temperature even more accurately. Since the pressure in the hollow cathode is the sum of the partial pressures of the electrons, ions, and neutrals, the experimental data presented in Figure 12 imply that either the gas is 40 to 50 percent ionized, or that the heavy particle temperature is between 2900 and 6100 ºC as listed in Table 2. The experimentally determined plasma properties support the latter conclusion as will be seen.

Cathode Temperature Distribution

The cathode temperature determined the means by which heat was lost to the surroundings and the upstream components of the assembly. By understanding the dominant heat transfer mechanisms, improvement of the cathode thermal isolation, and thereby performance, is facilitated. The model developed by Salhi[4] considered cathode operation in the limit of high power density where electron cooling was the only significant cooling mechanism. Since the focus of the present investigation was cathode operation in the limit of low-power density, additional cooling mechanisms were evaluated to determine their importance to the energy balance. A thermographic investigation was conducted to provide experimental data describing the significant heat transfer mechanisms at low-current.

Themographic Diagnostic Description

The experimental procedures are summarized here, and a detailed description of the thermography diagnostic appears in Domonkos, Gallimore, and Patterson.[25] The experimental set-up is depicted in Figure 15. An imaging radiometer scanned the infrared emissions from 8 to 12 μm. A close-up lens was added to the scheme shown in Figure 15 to enhance the resolution capabilities. The infrared image was downloaded to a computer where a commercially available image analysis software package was used to generate line profiles of pixel intensity which corresponded to temperature. Thermocouples were used to calibrate the radiometer output rather than relying on the built-in correction electronics included in the system. Sample images obtained with the radiometer are presented in Figure 16. The image in Figure 16a was adjusted to make the enclosed keeper visible. A slit was cut in the keeper so that the cathode surface temperature could be monitored. The slit width was approximately ten percent of the keeper diameter to permit the cathode surface to be viewed while minimizing the perturbation to the system. To resolve the cathode surface temperatures, the range on the radiometer was adjusted. Visible in Figure 16b are the cathode tube, heater, heater shield, and keeper. Note that the greyscales in Figure 16 are useful only for relative comparisons within a single image.

The line profiles presented here were all taken along the cathode axis. Figure 17 shows the raw data output from the imaging software. The length scale has already been adjusted. At the boundaries between the cathode tube and the heater radiation shield, the pixel data fail to reflect the same sharp transition in intensity expected with a step change in both temperature and emittance. This data artifact is characteristic of the imaging radiometer, and a more detailed discussion appears in Reference 25. The data from these transition locations are omitted when presenting the temperature profiles.

Infrared Imagery Derived Results

Qualitatively, the degree to which the temperature profile deviates from linearity indicates the relative importance of radiation heat transfer with respect to conduction. Several of the temperature profiles acquired in this investigation are plotted in Figure 18. The data markers represent the calibration locations for the thermocouples. All of these data were taken in a diode discharge with the keeper. At 0.50-A, the shape of the profiles appeared similar upstream of the radiation shields. The enclosed keeper cathode operated approximately 100 ºC higher at the tip. The slopes and slope changes in the profiles for both configurations are approximately equal beyond –12 mm upstream. Estimates limited the radiative transfer to about 0.4 W/cm of axial length at –12 mm, while the conduction was several Watts. Consequently, thermal conduction was found to be the dominant heat transfer mechanism in the upstream section of the tube at low-current. The resolution of the camera was insufficient to accurately determine the profile at the cathode tip. At 1.25-A and 1.50-A, the enclosed keeper upstream profiles were noticeably more linear than the open keeper distributions. By limiting the radiative transfer, the use of an enclosed keeper simplifies the problem of cathode optimization; minimizing the heat losses is accomplished by limiting thermal conduction. The profiles on the heater shield and the cathode tip temperatures followed the same trends throughout the current range tested. As is shown in the next section, the temperatures were weakly dependent upon on the flow rate, and the data presented in Figure 18 were representative of the distributions at all of the flow rates tested.

Tip Temperature Variations with Cathode Geometry

A disappearing filament optical pyrometer with emissivity correction was used to determine the orifice plate temperatures. The variation of the orifice plate temperatures with geometry, current, and flow rate is presented in Figure 19. The temperature was observed to scale in proportion with the aspect ratio. As the aspect ratio increases, the power loss in conducting current through the orifice also increases, leading to the observed temperature differences. Although not immediately apparent from Figure 19b, a reduction in the orifice diameter led to a curtailed operating regime. The AR3´ cathode was limited to approximately 2/3 the current of AR3. Figure 19c shows the orifice plate temperatures for EK6 and OK6 as a function of flow rate for three currents. In all cases the enclosed keeper operated at higher temperatures than the open keeper. Most of the data in Figure 19 showed a slight increase in temperature at the onset of plume mode, the lowest flow rate for each curve. The contributing factors are the bombardment of the orifice plate by ions created in the cathode-keeper gap, and increased power deposition to the anode, thereby altering the thermal radiation environment.

Evaluation of the Plasma Environment

Langmuir probe diagnostics were conducted in the emission plasma downstream of the keeper, in the cathode-to-keeper gap, and in the insert region of AR3 as part of this investigation. The temperature, number density, and character of the distribution of the plasma both internal and external to the hollow cathode influence the power deposition to the cathode surfaces and the keeper. The plasma properties also allow for accurate descriptions of the current conduction processes.[19] The insert plasma properties are important for understanding the power deposition to the insert, for providing an accurate description of the particle flux to the orifice entrance, and for determination of the parameters governing the cathode internal pressure. Measurement of the plasma properties in the orifice was considered infeasible with electrostatic probes. The mechanisms governing spot and plume mode operation can be discerned from the character of the plasma in the cathode-keeper gap. The emission plasma properties determine the ease of the charge transport to a secondary anode, ion beam, or ambient plasma.

Planar Langmuir probes were used for all of the results presented here. The probe diameters were chosen to be 2-mm in the emission plasma, 0.13-mm in the cathode-to-keeper gap, and 0.25-mm in the insert region, much larger than the expected Debye lengths and yet small enough to draw a negligible current in the electron saturation condition (~20 mA). Downstream of the keeper, one probe was placed with its face perpendicular to the flow from the cathode, and the other probe was oriented parallel with the flow. These probes are hereafter referred to as the axial and radial probes, respectively. The cathode assembly, complete with the secondary anode located 60 mm downstream of the keeper, was mounted to a linear translation stage which moved the assembly with respect to the probes. The probes were positioned on axis with the hollow cathode, and data were taken at 5-mm increments between 2 and 52-mm downstream of the keeper. The cathode-to-keeper gap of AR3 was increased to 4-mm to enable a planar Langmuir probe to be inserted radially into the gap. Again, the translation stage was used to move the cathode with respect to the probe. The test configuration dictated a fixed probe for the insert region, and axial resolution was only possible by replacement of the probe. The results presented here were from three such tests, and the reader should be aware that the radial location of the probe was confined by the insert and the alumina shield on the probe, but otherwise undetermined. The probes extended to 1.5, 0.7, and within 0.5-mm upstream of the orifice. The discharge appeared to be unaffected by the presence of any of the Langmuir probes.

The axial and radial probes, downstream of the keeper, were biased using a bipolar power supply with a triangular voltage ramp at a few Hz. The axial and radial probes were biased with respect to the secondary anode. The current was measured using a calibrated shunt resistor. A digital oscilloscope was used to record the probe current and voltage, and a computer acquisition system was used to download the I-V characteristics. A source meter was used to bias and measure the current-voltage characteristic of the internal probes and the cathode-to-keeper (CK) gap probe. The insert probes were ramped with respect to cathode potential, and the CK gap probe was biased with respect to the keeper. The source meter output the current and voltage of the probe directly to a computer via a GPIB connection.

Standard Langmuir probe analysis, assuming a Maxwellian plasma, was performed to reduce the data. The electron temperature was taken as the inverse slope of the natural log of the electron current near the floating potential. The plasma potential was taken as the probe voltage at the peak of the first derivative of the current. The electron number density was calculated based on the current at plasma potential for the axial and radial probe data. The ion saturation current was used to obtain the electron number density for the internal plasma.

In addition to the standard Langmuir probe analysis, the electron energy distribution functions were evaluated by examining the character of the second derivative of the probe current with respect to voltage. For an isotropic electron population, the second derivative of the probe current is approximately proportional to the electron energy distribution function (EEDF)[26,27]

$$f(E) \cong A\sqrt{E}\,\frac{d^2 I_{pr}}{dV_{pr}^2} \qquad \textbf{(6)}$$

where A is a normalization constant and the electron energy, E, is defined as

$$E = V_p - V_{pr} \qquad \textbf{(7)}$$

The second derivative of the probe current was obtained by numerical differentiation. Rundle, et al.[28] measured the electron energy distribution function in an O_2 glow discharge, and used the generaralized formula

$$f(E) = A\sqrt{E}\exp\left(-bE^{x}\right) \quad \textbf{(8)}$$

where A, b, and x are constants, to curve fit the distribution data. The case where x = 1 is the Maxwellian distribution, and when x = 2, Eqn. 8 yields the Druyvesteyn distribution. The coefficients in Eqn. 8 were determined by fitting the second derivative to an exponential with the argument E^x. The exponent, x, was allowed to vary between 1 and 2, and the correct value of x was determined by the quality of the fit. The coefficient b was determined directly from the fit, while A was determined by normalizing the distribution function.

In practice, it was necessary to fit the probe current and its first derivative to cubic splines so that the numerical differentiation yielded meaningful results; small random fluctuations at high values of E were magnified by the numerical differentiation and the factor of $E^{1/2}$ in Eqn. 8 in the absence of the cubic spline fits. Additionally, the plasma potential used in Eqn. 7 was the probe voltage at the peak of the second derivative of the probe current. This modification was chosen to yield a distribution function that more closely followed the form of Eqn. 8, and the difference in the value of the potential was typically less than 1-V. The nature of the Langmuir probe current-voltage characteristics were such that all of the best curve fits indicated a Druyvesteyn distribution, and an example is depicted in Figure 20. In each case, the second derivative reached its peak with a diminishing negative slope rather than the sharp peak indicative of a Maxwellian distribution. The derivative of a cubic spline accurately reflects a sharp change in slope only if sufficient points are included in the spline. Consequently, the EEDF data were used to examine the structure of any populations in the tail of the distribution and as a check of the electron temperature calculated using the standard Langmuir probe analysis.

The Emitted Plasma

Table 3 summarizes the operating conditions during the probe diagnostics. Since axial and radial Langmuir probes were used in this region, it was possible to assess the relative anisotropy of the emitted plasma; an isotropic plasma is also assumed in the classical Langmuir probe analysis. When no current is being extracted to the secondary anode, the ability of an electron to stream past the keeper is determined by its energy, and the temperature of the plasma increases with distance from the keeper. By extracting a current to the secondary anode, the net charge density in the gap is decreased, allowing lower temperature electrons to populate the space. However, by extracting a current, the axial electron energy is increased, and the degree of isotropy in the plasma is decreased. These effects can be seen in Figure 21. When the assembly was operated as a diode, the axial and radial temperatures differed by approximately 0.2 eV. As expected, the difference between the temperatures increased when electron current was extracted axially, indicating a higher degree of anisotropy. As a result of this analysis, the radial Langmuir probe data were considered to be more representative of the true plasma temperature, and only the results obtained with the radial probe are presented below.

A comparison of the electron temperatures in spot and plume modes is depicted in Figure 22. The spot mode electron temperatures were consistently less than 1 eV, while in plume mode, the electron temperature varied from approximately 1.5 to 2.5 eV. These results are consistent with the theory for spot and plume modes described in Reference 18. In spot mode, the ion flux to the keeper and beyond was sufficient to neutralize the space charge, and a low-energy population of electrons is emitted. When the ion flux becomes too small in plume mode, space charge limitations allowed only a high-energy electron population to escape. The high-energy electron population excites and ionizes the xenon at an increased rate, giving rise to the greatly increased light emission from the plasma. Figure 23 illustrates that as the secondary anode extracts a current, lower energy electron populations were obtained, although the change was only a few tenths of an electron volt. The electron temperatures immediately downstream of the keeper and immediately upstream of the secondary anode were invariant in these tests. The discharge with the secondary anode deposited energy into the emission plasma, raising the electron temperature near the anode. While the EEDFs appeared Druyvesteyn as shown in Figure 24, calculation of the average electron energy yielded results in agreement with the electron temperatures in Figure 22 and Figure 23.

The plasma potential data also illustrate the processes described above, as shown in Figure 25. In the case of zero current to the secondary anode, the plume-mode (0.50-A) plasma potential decayed rapidly downstream of the keeper, indicative of the low density plasma. In spot mode, the downstream plasma potential was nearly invariant with keeper current. The higher density spot-mode plasma was able to sustain a greater charge density than the plume-mode plasma. While the plasma potential generally decayed with increasing distance from the keeper, Figure 26 shows that during current extraction, the downstream potential leveled out and increased with the extraction

current. As the electrons were depleted from the plasma at the secondary anode, the potential was adjusted to facilitate current collection.

The electron number densities in the emission plasma are plotted in Figure 27. To summarize Figure 27, the number density increased with flow rate, keeper current, and emission current, and the densities approximately followed a cubic expansion with radius as expected. The keeper current appeared to have the strongest affect upon the downstream density. The emission electron number densities were one to two orders of magnitude lower than those observed in the very-near-field of the 1.35 kW D55 anode layer thruster.[29] Ion thruster beam densities are of the same order as those observed emitted from the hollow cathode.[30]

The Plasma in the Orifice and Cathode-Keeper Regions

Although the current density is greatest in the orifice and the plasma in the cathode-to-keeper gap greatly influences the onset of plume-mode, little experimental data have been taken in these regions using electrostatic probes, due to the small scales of the orifice and CK gap. To the authors' knowledge, the electron number density in the orifice has yet to be measured experimentally. To gain insight into the physical conditions within the orifice, the model developed by Mandell and Katz[19] was used. The electron density was calculated to vary from 5×10^{14} to 1×10^{16} cm^{-3} for the geometries and test conditions in this investigation. At this density, with electron temperatures of up to 2.5 eV, the electrons, ions, and neutrals undergo several thousand collisions along the length of the orifice. The collisional heating of the ions by electrons significantly increases the heavy particle temperature.[4] This is the mechanism responsible for the elevated pressures observed in Figure 12 during cathode operation. A more detailed presentation of this phenomenon appears in Reference 31. Experimental Laser Induced Fluorescence (LIF) data indicated that the neutral temperatures in the cathode-keeper gap were between 1800 and 4000 K in approximate agreement with values estimated in Table 2.[31]

Plasma potential data were sought by Williams et al.[31] in order to explain ion velocities observed by LIF. The plasma parameters in the CK gap are presented in Figure 28. Both cases at 1 sccm were plume mode, while the condition at 3 sccm was spot mode. Only the potentials for two of the conditions are reported in Figure 28 because the noise associated with plume mode operation made it difficult to determine the plasma potential accurately. The potential variation in spot mode supports the notion that charge neutralization in the gap was maintained, while in plume mode, the plasma was more highly negative with respect to the keeper, thereby creating a more favorable condition for ions to maintain quasineutrality. The electron temperature distributions also corroborated this explanation; the increased electron temperature in plume mode was a manifestation of the onset of space-charge limitations to the electron flow. The electron number density varied from 3×10^{12} to 2×10^{13} cm^{-3}. The error on the number density was calculated to be approximately ±60 percent. The density decreased with diminishing flow rate, dwindling current, and axial distance from the cathode.

Figure 29 depicts the spot mode electron energy distribution functions in the cathode-to-keeper gap. The bulk of the electrons formed a distribution that approximated a Druyvesteyn distribution to 1.5 eV. Between 1.5 and 4 eV, the tail of the distribution appeared inflated. The tail decayed with axial distance from the orifice, indicating that collisional events were driving the distribution toward equilibrium. The decrease in electron energy with axial distance from the orifice was also apparent in Figure 28. Although the EEDFs were Druyvesteyn, the average electron energy was approximately 1.5 times the calculated electron temperatures, again showing agreement between the two measurements.

The Plasma in the Insert Region

Both Siegfried[3] and Salhi[4] have measured the plasma properties in the insert region of 6.4 mm outer diameter hollow cathodes, and despite the different propellants, both measured similar temperatures, potentials, and number densities. The goal in the present investigation was to verify that the plasma properties were of the same order as those measured by Siegfried[3] and Salhi.[4]

The axial variation of the plasma properties with flow rate is plotted in Figure 30. The plasma potential rose slightly with decreasing flow rate and more strongly as the orifice was approached. The potential values and the trends were similar to those observed by Salhi.[4] The plasma property variation with current 0.7 mm upstream of the orifice is depicted in Figure 31. Here the plasma potential was observed to decrease with increasing current, again similarly

to the data taken by Salhi.[4] As shown for the external plasmas, the electron temperature in spot mode generally remained below 1 eV in the insert region as well. The electron temperature was observed to increase as the current was increased. The axial variation in the plasma number density shown in Figure 30 exhibited a much sharper gradient than that observed by either Siegfried[3] or Salhi.[4] Otherwise, the number density data followed the same trends and were approximately equal in peak magnitude to the data by Siegfried.[3] Salhi[4] measured the plasma number density to be a factor of five higher in magnitude than those reported here. The tendency of the high neutral density within the insert region will be to quench the discharge, and the sharp gradients in number density reported here reflect that intuition.

Discussion of Low-current Hollow Cathode Applications

Given the preceding presentation of the state of hollow cathode development, it is useful to consider the ways in which these cathodes fulfill the requirements of low-power electric propulsion systems. Ion thrusters in the 100-300 W range consume approximately 1.5 to 3 sccm of xenon in the discharge chamber, while comparable Hall thrusters require 5 to 15 sccm.[1,32] In each case, the cathode flow substantially reduces the specific impulse and efficiency, and the keeper discharge power consumes a more significant fraction of the total when compared to kW-class thrusters. Hall thrusters may be operated without a keeper, mitigating the power loss in this discharge. However, given the likely discharge current for a 100 to 300 W Hall thruster, the self-heating due to the discharge may be insufficient to sustain cathode operation. For ion thrusters, the neutralizer keeper must be operated while thrusting to sustain the discharge.

This paper investigated the temperature profiles in low-power hollow cathodes to provide evidence indicating the dominant heat transfer mechanisms. Findings of previous works[3,4,9] indicated that the extreme downstream end of the insert receives the bulk of the power deposition to the insert. The model by Mandell and Katz[19] predicts that high plasma density in the orifice leads to power deposition to the orifice plate on the order of several Watts. The experimental results presented here agreed with the findings of these previous investigations. Further, the effectiveness of the enclosed keeper as a radiation shield was quantified. With the enclosed keeper, conduction was determined to be the dominant heat transfer mechanism from the high-temperature end of the cathode. Since conduction dominated the heat transfer in the low-current hollow cathodes, the use of a low thermal conductivity material should enable elevated temperatures on the emitter at low-currents. The materials used in this investigation were chosen primarily for their strength at high temperature, low sputter yield, low oxygen content and adsorbtion, and heritage in hollow cathodes. Cathode optimization is accomplished partially by carefully selecting cathode materials which have a low sputter yield, low thermal conductivity, and favorable high temperature properties. The elaborate cleaning procedures and the immaculate propellant feed systems currently used with hollow cathodes have minimized the introduction of contaminants to the emitter. Consequently, the material choices were reevaluated, and Table 4 summarizes the benefits of several candidate materials.[33] The emissivity varies only slightly between the materials listed. Niobium and titanium offer the most substantial improvements compared with the current state-of-the-art, and are suggested for future investigations. By improving the thermal environment for thermionic electron emission, the ion production rate and efflux from the orifice should increase, leading to a reduction in the flow rate for spot-mode operation.

While the electrical efficiency of the Space Technology 4 NSTAR ion thrusters and the ISS plasma contactors is sufficient, expellant requirements for their respective missions yield lower than desired propellant margin. Similarly low-power electric propulsion would also benefit greatly from a reduction in the cathode flow rate. In addition to increasing the orifice length to reduce the spot-mode flow rate mentioned previously, additional work by Katz[34] examined the path for ions emitted from the orifice. The premise is to maximize the number of ions created at the downstream edge of the ionization region that maintain charge neutralization versus those that are lost to cathode surfaces. By minimizing the solid angle of cathode surface seen by the ions, charge neutralization in the cathode-keeper gap is facilitated. Since the orifice chamfer was implemented in response to the observed erosion pattern of cathodes operated primarily in plume-mode, elimination of the chamfer, thereby reducing orifice plate thickness, for spot-mode operation is the most straightforward modification to accommodate ion transport. Additional modifications to the orifice plate and keeper geometry can further optimize ion transport. Taking into account a number of these recommendations, a second-generation laboratory model cathode was fabricated, and preliminary results have shown significant power and flow-rate reductions for spot-mode operation.

Conclusions

This paper described an extensive experimental investigation targeting the operational drivers which determine the effectiveness of hollow cathodes for low-power electric propulsion. Five separate 3.2 mm diameter orificed hollow cathodes were designed and tested in a number of different configurations. After establishing the performance variance between mechanically identical cathodes, power and expellant consumption were evaluated for several different orifice and keeper geometries. Power consumption increased with orifice length, while the minimum flow rate decreased. Both of these findings were predicted by the model described in Reference [19]. The use of an enclosed keeper reduced the power consumption, however the minimum flow rate was observed to increase. The latter finding was unexpected because the use of an enclosure increases the local pressure in the cathode-keeper gap, which should lead to increased ion creation and transport with the electrons downstream. The cathode internal pressure was found to vary from 39.2 to 66.5 kPa in spot mode, and the transition to plume mode occurred at a nearly fixed internal pressure regardless of the current or flow rate. Subsequent analysis of the insert plasma with Langmuir probes and the cathode-to-keeper plasma suggested that several tens of kPa were possible only if the heavy particle temperature was on the order of several thousand degrees C. LIF measurements by Williams, et al.[31] indicated that the neutral temperatures were several thousand degrees C.

The behavior of the cathode external temperatures was also studied to determine the important heat transfer modes. Conduction dominated the heat transfer from the cathode surface. The condition was more pronounced when an enclosed keeper was used. This conclusion means that cathode performance at low-power can be readily improved by choosing materials with a low thermal conductivity for cathode construction. A brief discussion of possible material choices was presented.

Finally, plasma parameters were measured in the insert region, in the cathode-to-keeper gap, and downstream of the keeper. These data were intended to provide validation for a cathode model currently under development. While the dimensions in this investigation precluded detailed mapping similar to Salhi,[4] the resolution was sufficient to compare the plasma properties in the 3.2-mm orificed hollow cathodes with those measured by others.[3,4] The electron number density in the insert was of the same order, and exhibited a sharper gradient near the orifice than the data by Siegfried.[3] The electron temperature in spot mode was consistently less than 1 eV, while the onset of plume mode led to electron temperatures above 1 eV. The number density in all regions scaled with the flow rate and the current. The anisotropy of the plasma downstream of the keeper was found to increase with beam extraction. The electron energy distribution function was also measured to validate the parameters determined using the standard Langmuir probe analysis. While the distribution functions all appeared to be Druyvesteyn, the calculated average electron energies agreed well with the previously determined electron temperatures.

Acknowledgements

This work was supported by NASA GRC Grant No. NGT-3-52311. The authors greatly appreciate the invaluable assistance provided by Michael Pastel, Ralph Jacko, Robert Roman, John Foster, George Soulas, and Timothy Sarver-Verhey at GRC, and Tim Smith and Karyl Shand at PEPL.

References

[1] Patterson, M. J. and Oleson, S. R., "Low-Power Ion Propulsion for Small Spacecraft," AIAA Paper No. 97-3060, 33rd AIAA / ASME / SAE / ASEE Joint Propulsion Conference, July 1997, Seattle, WA.

[2] Rawlin, V. K., "A 13,000 Hour Test of a Mercury Hollow Cathode," NASA TM X-2785, 1973.

[3] Siegfried, D. E., A Phenomenological Model for Orificed Hollow Cathodes, Ph.D. Dissertation, Colorado State University, 1983.

[4] Salhi, A., Theoretical and Experimental Studies of Orificed, Hollow Cathode Operation, Ph.D. Dissertation, Ohio State University, 1993.

[5] Rawlin, V. K. and Pawlik, E. V., "A Mercury Plasma-Bridge Neutralizer," *Journal of Spacecraft and Rockets*, Vol. 5, No. 7, July 1968, pp. 814-820.

[6] Byers, D. C. and Snyder, A., "Parametric Investigation of Mercury Hollow-Cathode Neutralizers," *Journal of Spacecraft and Rockets*, Vol. 8, No. 2, Feb. 1971, pp. 133-139.

[7] Rawlin, V. K. and Kerslake, W. R., "Durability of the SERT II Hollow Cathodes and Future Applications of Hollow Cathodes," AIAA Paper No. 69-304, AIAA 7th Electric Propulsion Conference, Williamsburg, VA, Mar. 1969.

[8] Mirtich, M. J., "Investigation of Hollow Cathode Performance for 30-cm Thrusters," NASA TM X-68298, 1973.

[9] Goldstein, R., Pawlik, E. V., and Wen, L.-C., "Preliminary Investigations of Ion Thruster Cathodes," JPL Technical Report 32-1536, 1971.

[10] Ferreira, C. M. and Delcroix, J. L., "Theory of the Hollow Cathode Arc," *Journal of Applied Physics*, Vol. 49, No. 4, April 1978, pp. 2380-2395.

[11] Sarver-Verhey, T. R., "Destructive Evaluation of a Xenon Hollow Cathode After a 28,000 Hour Life Test," NASA/CR—1998-208678.

[12] Soulas, G. C., "Multiple Hollow Cathode Wear Testing," NASA Contractor Report 195335, June 1994.

[13] Fearn, D. G. and Philip, C. M., "An Investigation of Physical Processes in a Hollow Cathode Discharge," AIAA Paper No. 72-416, AIAA 9th Electric Propulsion Conference, Bethesda, MD, April 1972.

[14] Rehn, L. A., "Argon Hollow Cathode," NASA CR-135102, Nov. 1976.

[15] Rehn, L. and Kaufman, H. R., "Correlation of Inert Gas Hollow Cathode Performance," AIAA / DGLR 13th International Electric Propulsion Conference, San Diego, CA, April 1978.

[16] Patterson, M. J., Verhey, T. R., Soulas, G., and Zakany, J., "Space Station Cathode Design, Performance, and Operating Specifications," IEPC Paper No. 97-170, 25th International Electric Propulsion Conference, Cleveland, OH, Aug. 1997.

[17] Sarver-Verhey, T. R., "Extended Test of a Xenon Hollow Cathode for a Space Plasma Contactor," NASA Contractor Report 195402, Nov. 1994.

[18] Kaufman, H. R., "Technology of Electron-Bombardment Ion Thrusters," *Advances in Electronics and Electron Physics*, Vol. 36, 1974, pp. 265-373.

[19] Mandell, M. J. and Katz I., "Theory of Hollow Cathode Operation in Spot and Plume Modes," AIAA Paper No. 94-3134, 30th AIAA / ASME / SAE / ASEE Joint Propulsion Conference, Indianapolis, IN, June 1994.

[20] Sarver-Verhey, T. R., "28,000 Hour Xenon Hollow Cathode Life Test Results," IEPC Paper No. 97-168, *25th International Electric Propulsion Conference*, Cleveland, OH, Aug. 1997.

[21] Suitch, P. R., Thermochemical Reactions in Tungsten-Matrix Dispenser Cathodes Impregnated with Various Barium-Calcium-Aluminates, Ph.D. Thesis, Georgia Institute of Technology, 1987.

[22] Domonkos, M. T., Gallimore, A. D., and Patterson, M. J., "An Evaluation of Hollow Cathode Scaling to Very Low-power and Flow Rate," IEPC Paper No. 97-189, *25th International Electric Propulsion Conference*, Cleveland, OH, Aug. 1997.

[23] Domonkos, M. T., Gallimore, A. D., and Patterson, M. J., "Parametric Investigation of Orifice Aspect-Ratio Effects on Low-Current Hollow Cathode Power Consumption," AIAA Paper No. 98-3345, *34th AIAA / ASME / SAE / ASEE Joint Propulsion Conference*, Cleveland, OH, July 1998.

[24] White, F. M., *Viscous Fluid Flow*, McGraw-Hill, Inc., New York, 1991.

[25] Domonkos, M. T., Gallimore, A. D., and Patterson, M. J., "Thermographic Investigation of 3.2-mm-Diameter Orificed Hollow Cathodes," AIAA Paper No. 98-3793, *34th AIAA / ASME / SAE / ASEE Joint Propulsion Conference*, Cleveland, OH, July 1998.

[26] Druyvesteyn, M. J., *Z. Physik*, Vol. 64, pp. 781, 1930.

[27]Swift, J. D. and Schwar, M. J. R., Electrical Probes for Plasma Diagnostics, American Elsevier Publishing Company, Inc., New York, 1970.

[28] Rundle, H. W., Clark, D. R., and Deckers, J. M., "Electron Energy Distribution Functions in an O_2 Glow Discharge," *Canadian Journal of Physics*, Vol. 51, pp. 144-148, 1973.

[29] Domonkos, M. T., Marrese, C. M., Haas, J. M., and Gallimore, A. D., "Very Near-Field Plume Investigation of the D55," AIAA Paper No. 97-306, 33rd *AIAA / ASME / SAE / ASEE Joint Propulsion Conference*, Seattle, WA, July 1997.

[30] Jansen, S. W., "Microwave Diagnostics for Ion Thrusters," IEPC Paper No. 93-237, *23rd International Electric Propulsion Conference*, Seattle, WA, Sept. 1993.

[31] Williams, G., Smith, T., Domonkos, M., Shand, K., and Gallimore, A., "Laser Induced Fluorescence Characterization of Ions Emitted from a Hollow Cathode," AIAA Paper 99-2862, *35th AIAA / ASME / SAE / ASEE Joint Propulsion Conference*, Los Angeles, CA, June 1999.

[32] Patterson, M. J., Grisnik, S. P., and Soulas, G. C., "Scaling of Ion Thrusters to Low-power," IEPC Paper No. 97-098, *25th International Electric Propulsion Conference*, Cleveland, OH, Aug. 1997.

[33] Matsunami, N., et al., "Energy Dependence of the Ion-Induced Sputtering Yields of Monatomic Solids," *Atomic Data and Nuclear Data Tables*, Vol. 31, No. 1, July 1984, pp. 1-80.

[34] Katz, I. and Patterson, M. J., "Optimizing Plasma Contactors for Electrodynamic Tether Missions," Tether Technology Interchange, Huntsville, AL, Sept. 1997.

Table 1 – Cathode Names and Configuration (Orifice Plate Dimensions Normalized by the AR6 Orifice Diameter)

Cathode	Normalized Orifice Diameter	Normalized Orifice Length	Keeper Type	Secondary Anode
AR6	1.0	5.6	Open	No
AR6´	1.0	5.6	Open	No
AR3	1.0	3.2	Open and Mesh	Yes, for Plasma Property Tests
AR3´	0.6	3.0	Open	No
AR1	1.0	1.4	Open	No
OK6	1.0	5.6	Open	No
EK6	1.0	5.6	Enclosed	Yes

Table 2 - Calculated Heavy Particle Temperatures to Match Cathode Internal Pressure Data

Current (A)	Heavy Particle Temperature (K)
0.50	2900
0.75	4300
1.00	5400
1.25	5800
1.50	6100

Table 3 - Cathode Operating Conditions for the Emission Plasma Parameters

Figures	Keeper Current (A)	Keeper Voltage (V)	Anode Current (A)	Anode Voltage (V)	Flow Rate (sccm)	Mode
Figure 22, Figure 25	0.50	18.60	0.00		2.4	Plume
Figure 22, Figure 27	0.75	24.42	0.00	1.31	1.3	Plume
Figure 22, Figure 23, Figure 21, Figure 25, Figure 26, Figure 27	0.75	17.20	0.00	2.30	2.4	Spot
Figure 27	0.75	17.05	0.00		3.3	Spot
Figure 22, Figure 25, Figure 27	1.50	15.75	0.00	5.78	2.4	Spot
Figure 23. Figure 26, Figure 27	0.75	17.28	0.17	20.00	2.4	Plume
Figure 23, Figure 21, Figure 26, Figure 27	0.75	16.52	0.30	24.22	2.4	Spot

Table 4 - Alternative Material for the Cathode Tube and Orifice Plate

Material	Melting Point (K)	Advantages	Disadvantages
Tantalum	3269	Moderate thermal conductivity, low coefficient of thermal expansion, extensively tested.	Moderate sputter yield for xenon, brittleness at high temperature.
Niobium	2741	Moderate thermal conductivity, low coefficient of thermal expansion, low sputter yield for xenon.	Lack of testing heritage, limited availability.
Titanium	1941	Low thermal conductivity, low sputter yield for xenon, readily available.	Moderate coefficient of thermal expansion, lack of test heritage, relatively low melting point.
Tungsten (also 2% Thoriated Tungsten)	3653	Low sputter yield for xenon, readily available, extensively tested.	High thermal conductivity.
Molybdenum	2883	Low sputter yield for xenon, readily available, extensively tested.	High thermal conductivity.

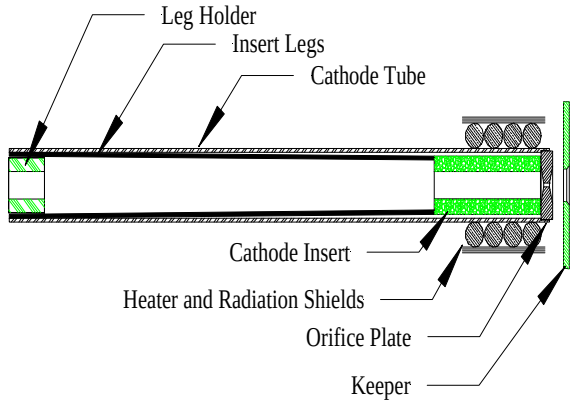

Figure 1 - Detailed Schematic of the Prototype Cathodes

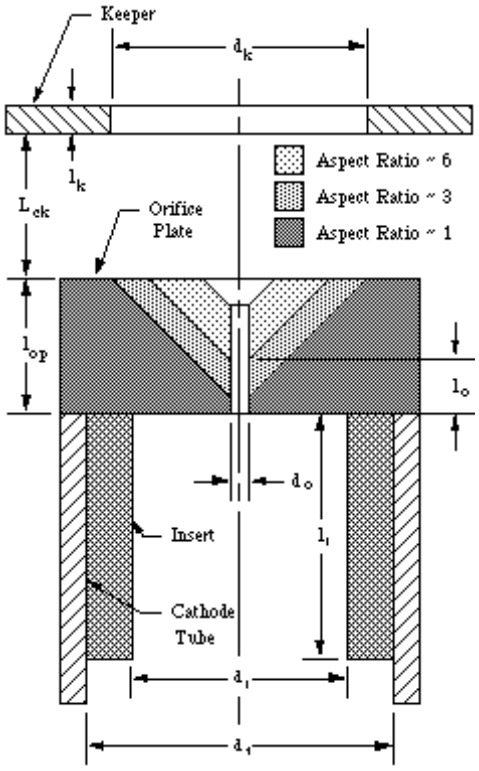

Figure 2 - Schematic of the Various Orifice Aspect Ratios

Figure 3 - Laboratory Model Removable Enclosed Keeper

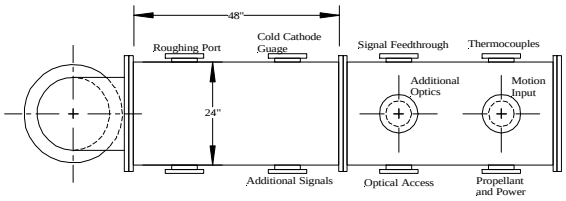

Figure 4 - Schematic of the Cathode Test Facility at The Plasmadynamics and Electric Propulsion Laboratory

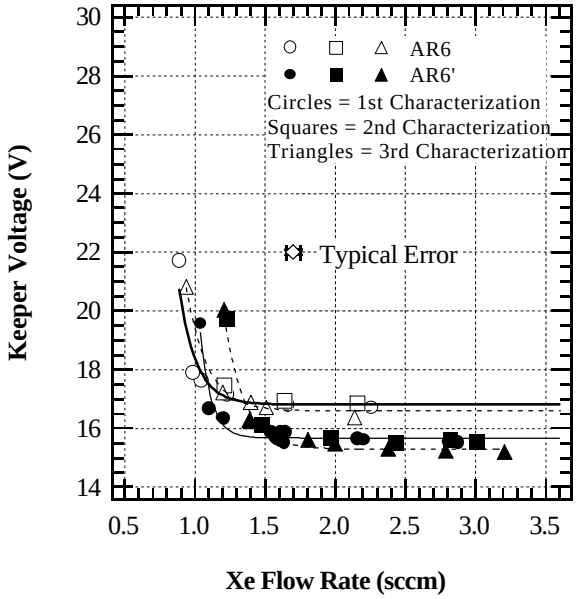

Figure 5. Performance Variance at 1.25-A for Three Mechanically Identical Hollow Cathodes

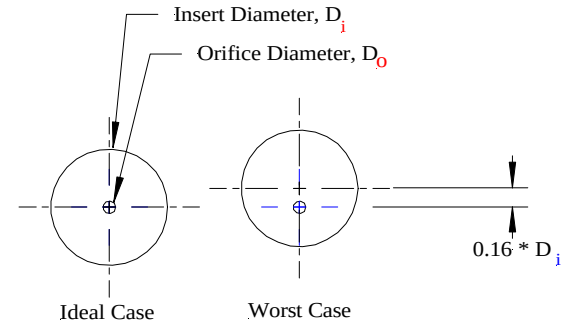

Figure 6. Illustration of the Maximum Possible Misalignment of the Orifice and Insert Axes

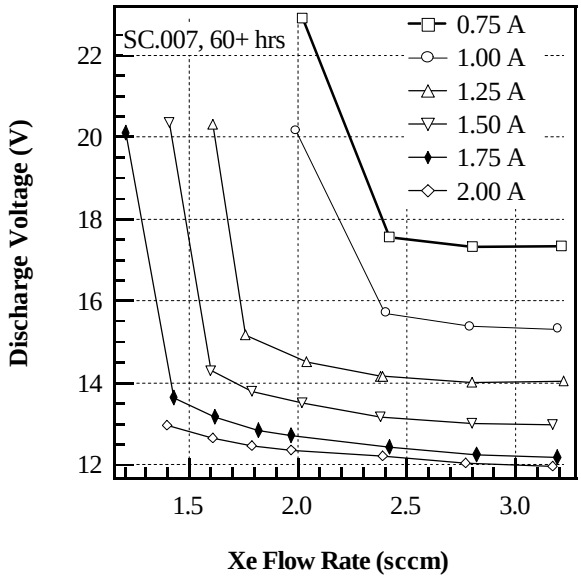

Figure 7 - Performance Characteristics of AR1 after 60 Hours of Operation

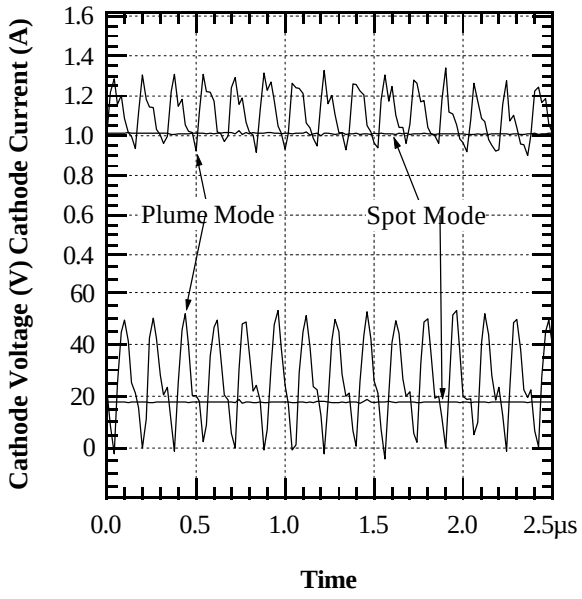

Figure 8 - Time Resolved Current-Voltage in Spot- and Plume-Mode for AR3

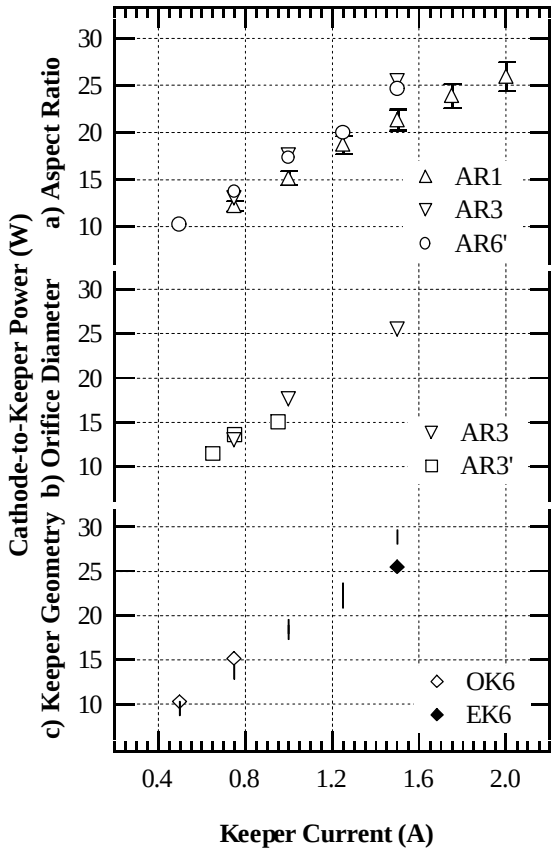

Figure 9 - Power Consumption at the Minimum Flow Rate for Spot-Mode Operation

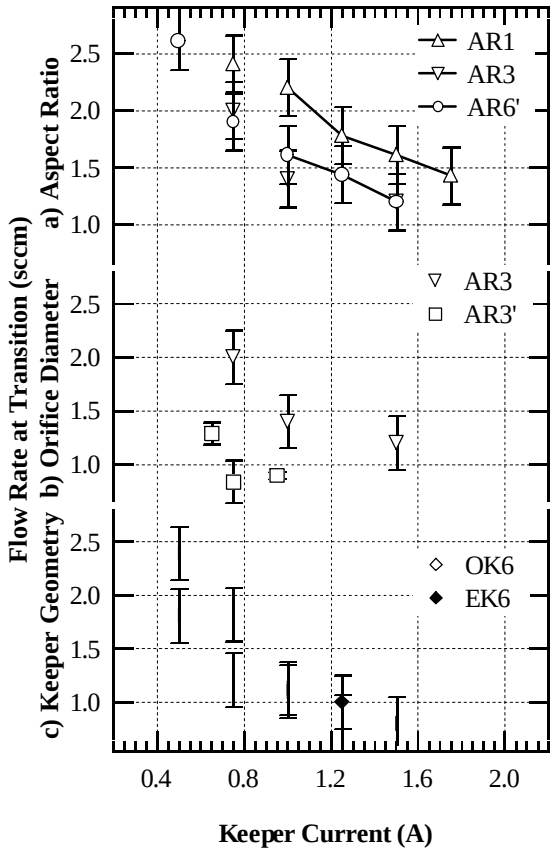

Figure 10 - Minimum Flow Rate for Spot-Mode Emission

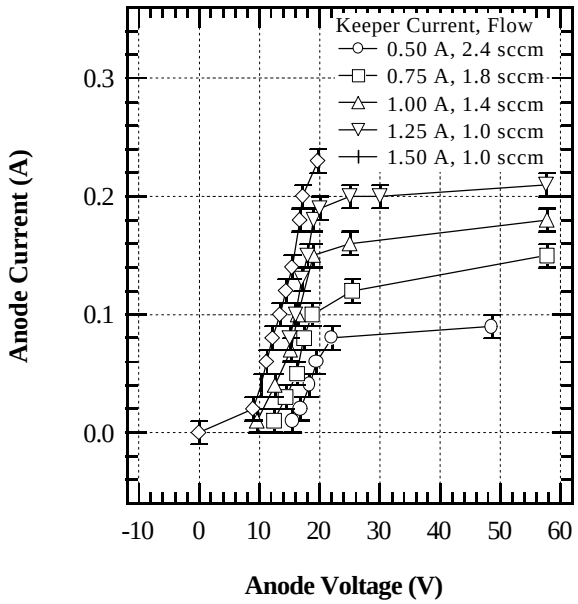

Figure 11 - Current Emission Characteristics to a Secondary Anode for the Enclosed Keeper Cathode

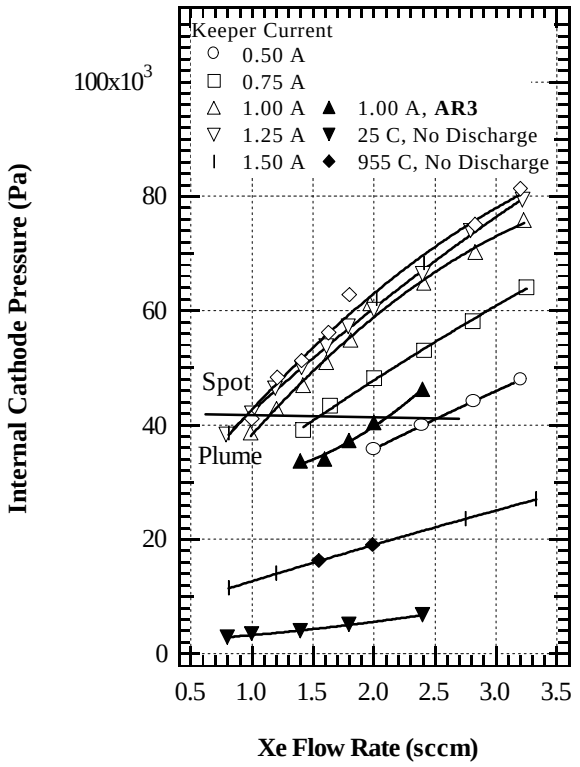

Figure 12 - Cathode Internal Pressures for EK6 and AR3

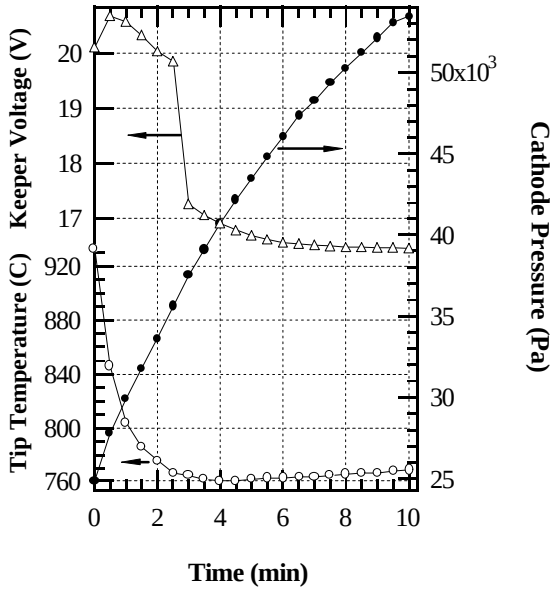

Figure 13 - Cathode Internal Pressure Start-Up Transient

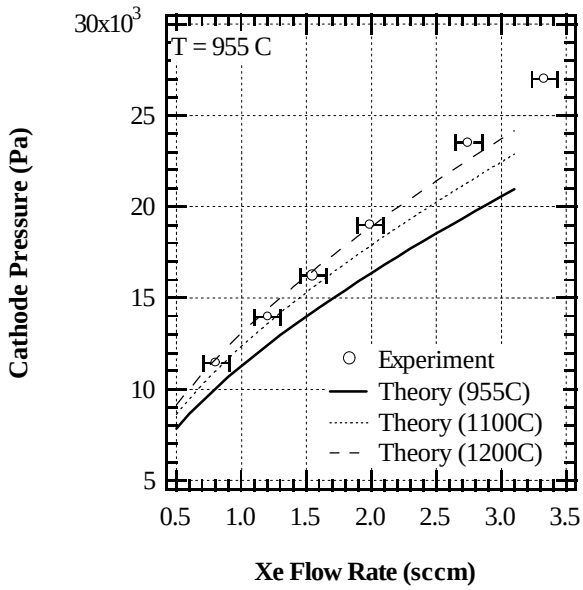

Figure 14 - Comparison of Cathode Pressure Model with Experiment (No Discharge)

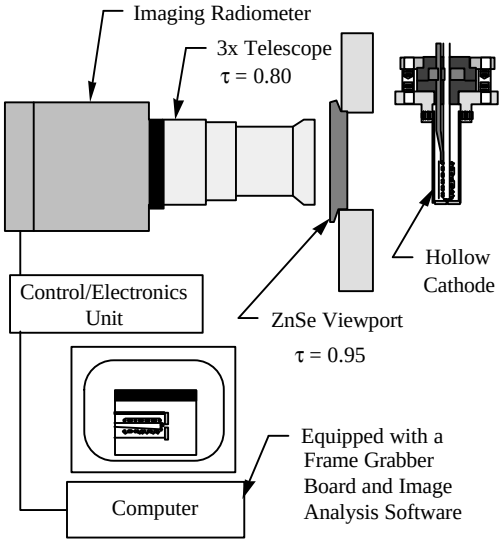

Figure 15 - Thermography Experiment Schematic

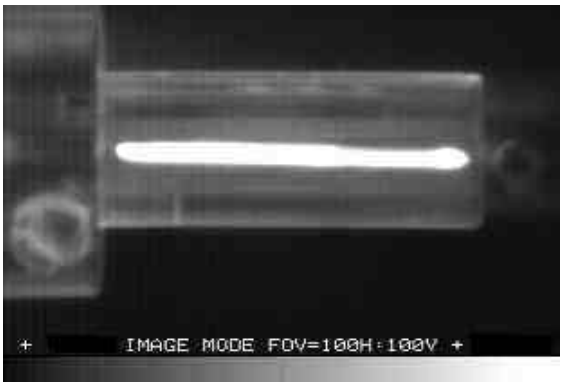

a) Enclosed Keeper Thermal Image

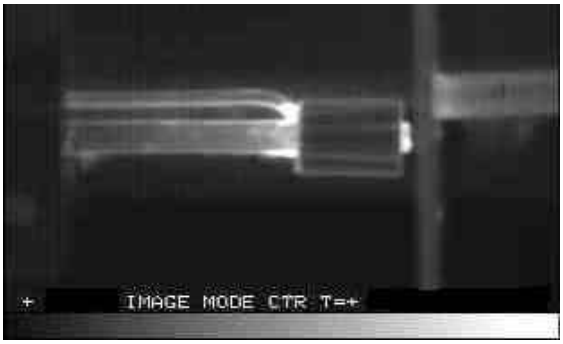

b) Open Keeper Thermal Image

Figure 16 - Sample Infrared Images from the Imaging Radiometer

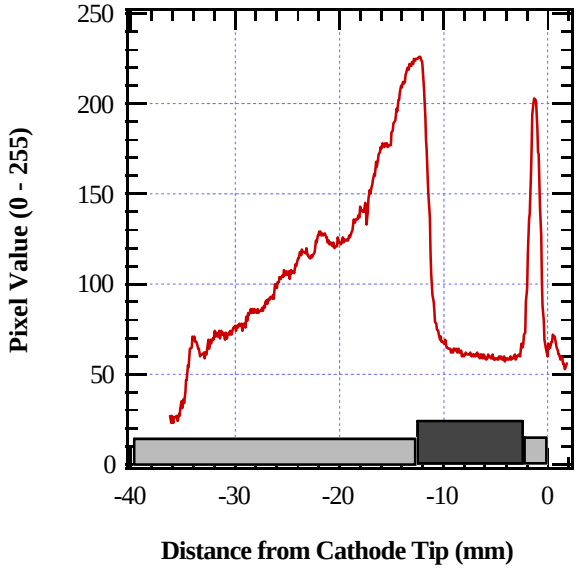

Figure 17 - Illustration of the Results of a Line Profile Along the Cathode Tube During Operation

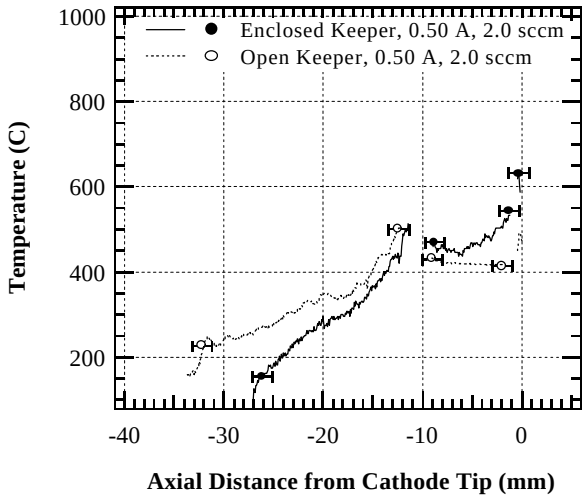

a) 0.50-A to Keeper

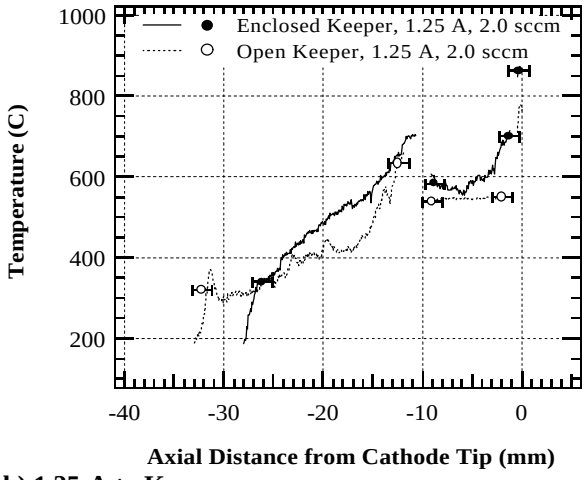

b) 1.25-A to Keeper

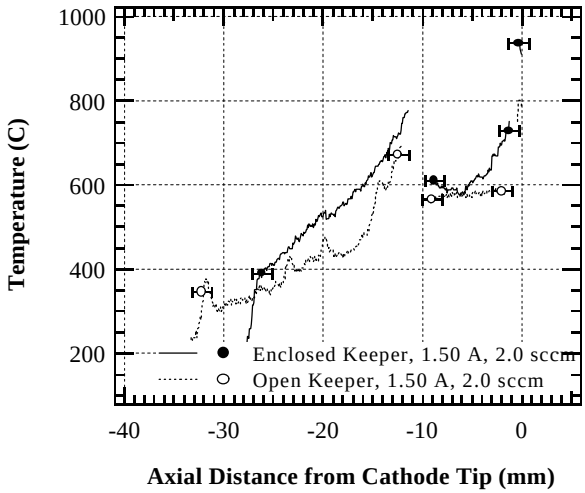

c) 1.50-A to Keeper

Figure 18 - Axial Temperature Profiles for the Open and Enclosed Keeper Configurations

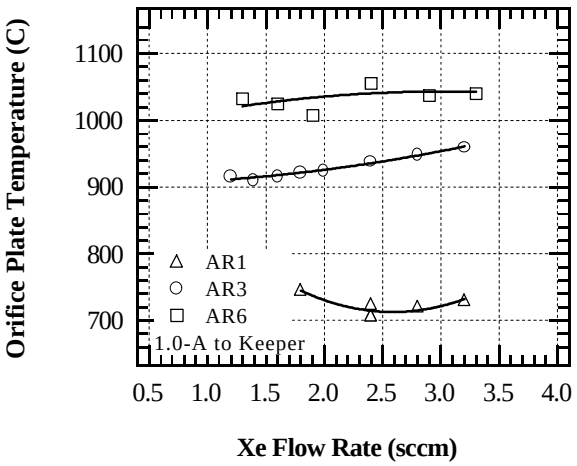

a) Aspect-Ratio Dependency

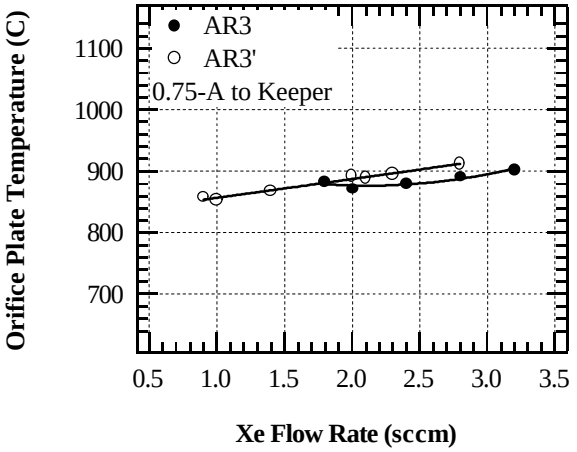

b) Orifice Diameter Dependency

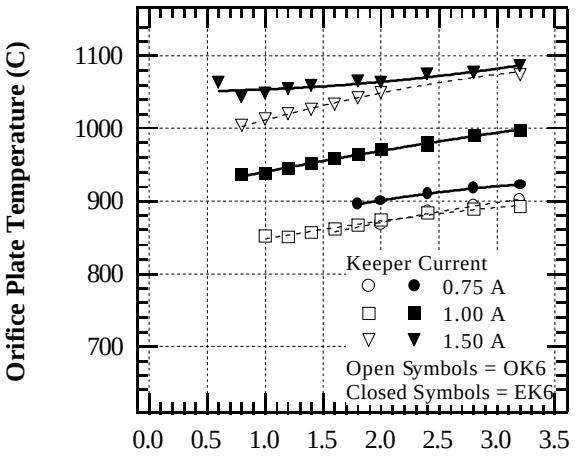

c) Keeper Geometry Dependency

Figure 19 - Pyrometer Observed Orifice Plate Temperatures for Several Geometries

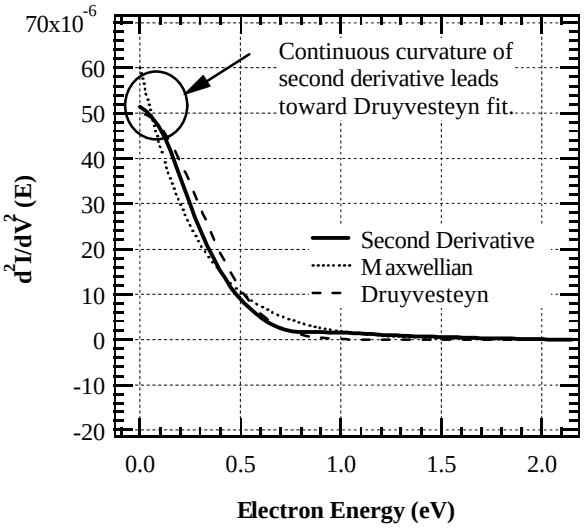

Figure 20 - Illustration of the Second Derivative of the Probe Current in Contrast to Maxwellian and Druyvesteyn Curve Fits

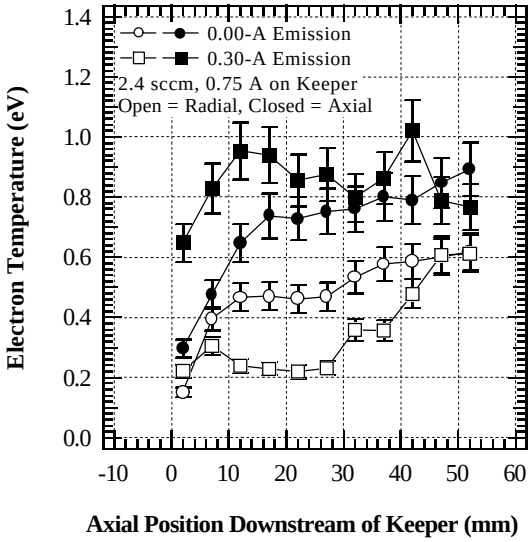

Figure 21 - Variation in Observed Electron Temperatures in the Radial and Axial Directions

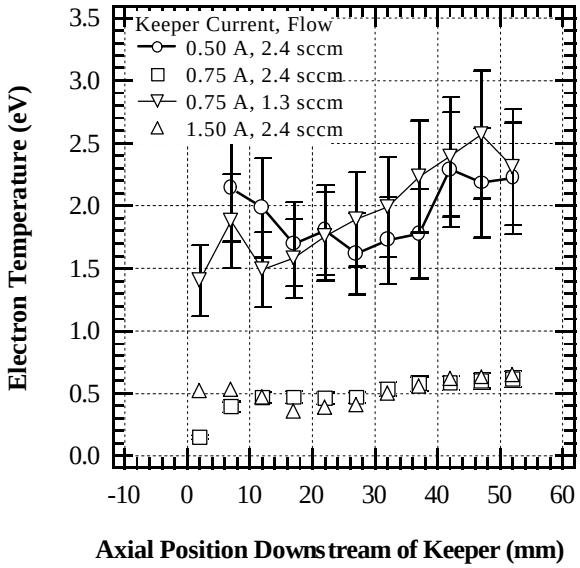

Figure 22 - Emission Plasma Electron Temperature In Spot and Plume Mode

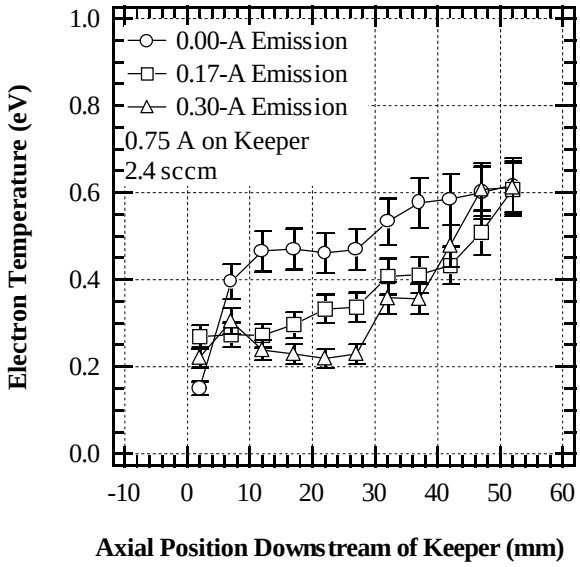

Figure 23 - Emission Plasma Electron Temperature with Electron Extraction

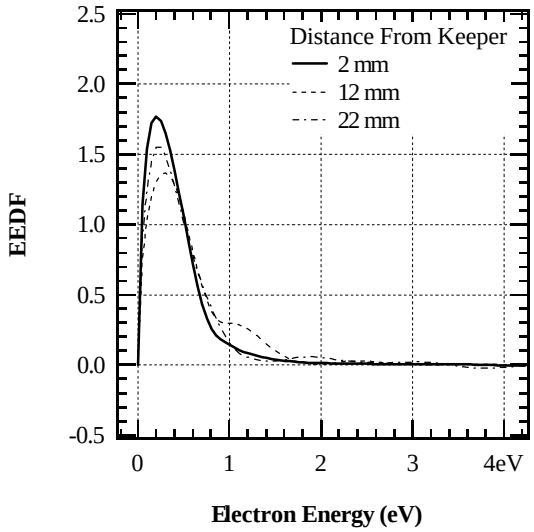

Figure 24 - Electron Energy Distribution Function Downstream of the Keeper at 0.75 A and 2.4 sccm.

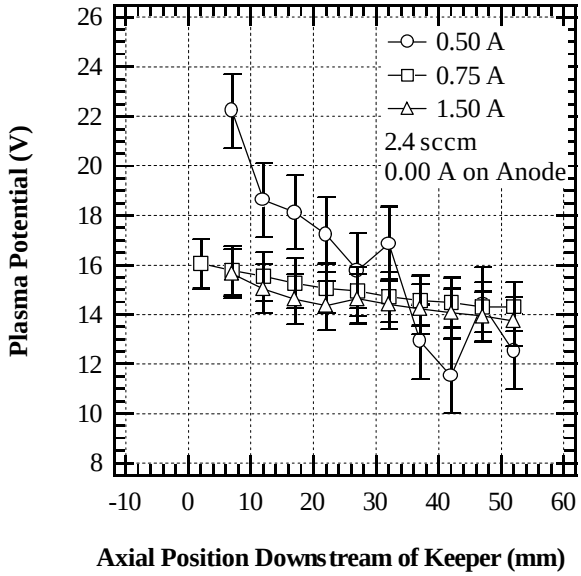

Figure 25 - Potential Variation in the Emission Plasma

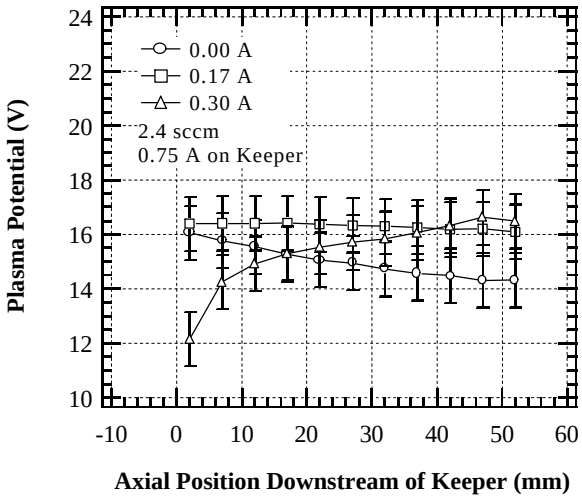

Figure 26 - Potential Variation While Extracting Current Downstream.

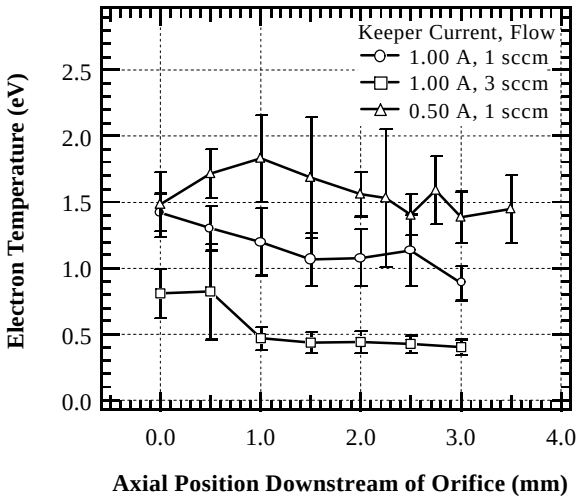

a) Electron Temperature

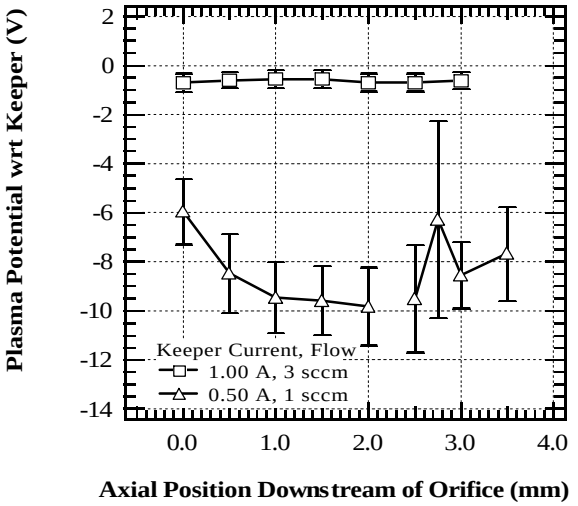

b) Plasma Potential

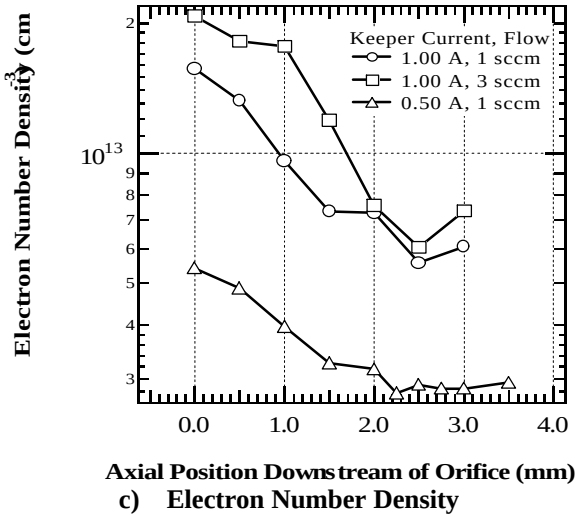

c) Electron Number Density

Figure 28 – Cathode – Keeper Gap Plasma Parameter Variation for Several Conditions

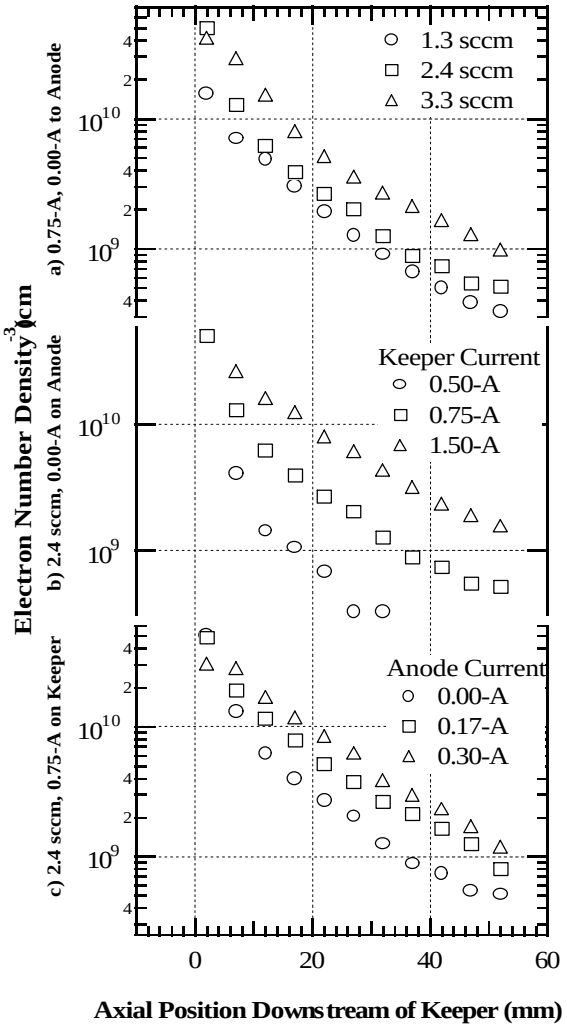

Figure 27 - Emission Electron Number Density

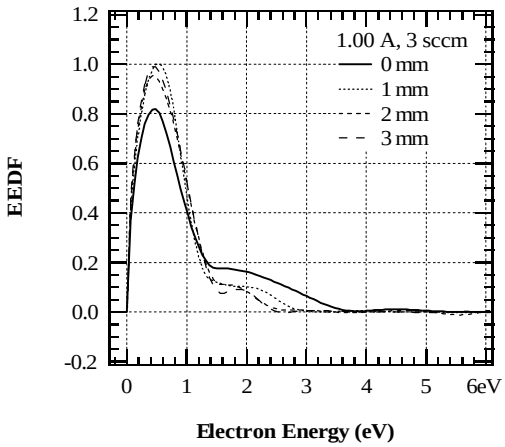

Figure 29 - Electron Energy Distribution Functions in the Cathode-Keeper Gap

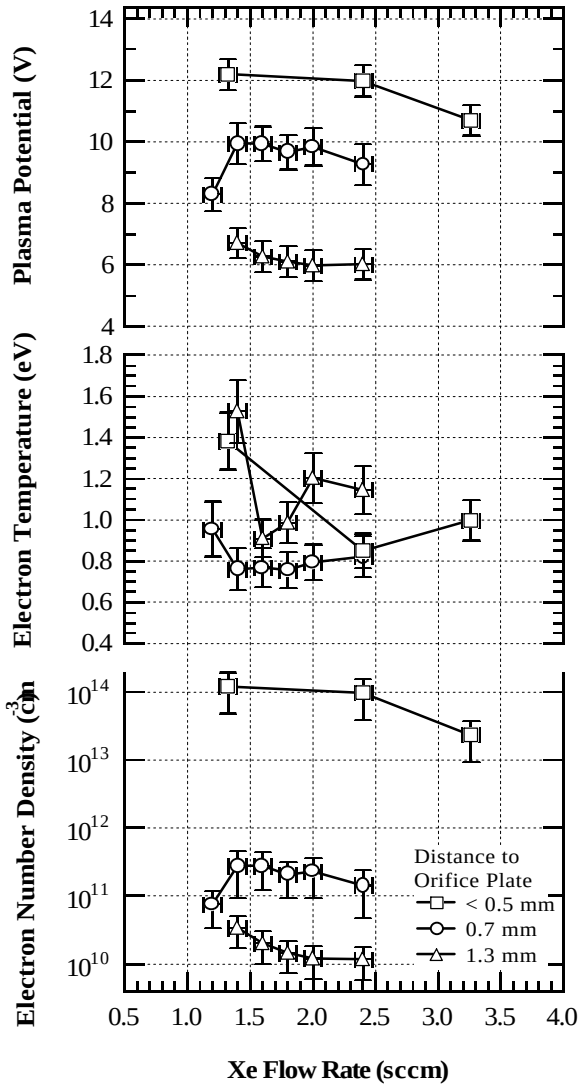

Figure 30 - Variation of Plasma Parameters in the Insert Region at 0.75 A Keeper Current.

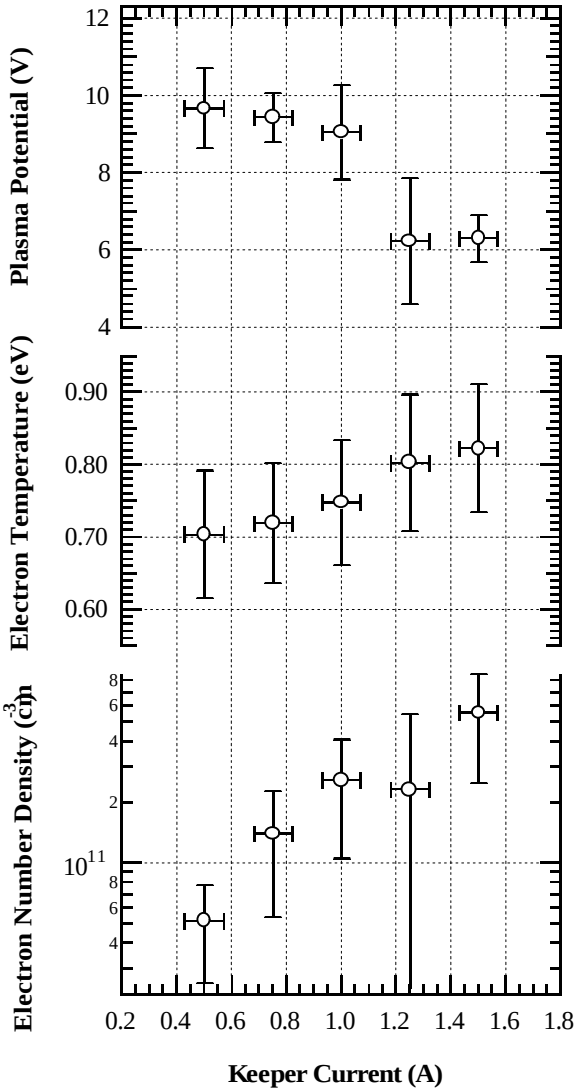

Figure 31 - Variation of Insert Region Plasma Parameters with Flow Rate 0.7 mm Upstream of the Orifice Plate